Shock-driven amorphization and melting in Fe_2O_3

Céline Crépisson,[1,*] Alexis Amouretti,[2,3] Marion Harmand,[4,5] Chrystèle Sanloup,[2] Patrick Heighway,[1] Sam Azadi,[1] David McGonegle,[6] Thomas Campbell,[1] Juan Pintor,[2] David Alexander Chin,[7] Ethan Smith,[7] Linda Hansen,[7] Alessandro Forte,[1] Thomas Gawne,[1] Hae Ja Lee,[8] Bob Nagler,[8] YuanFeng Shi,[1] Guillaume Fiquet,[2] François Guyot,[2] Mikako Makita,[9] Alessandra Benuzzi-Mounaix,[10] Tommaso Vinci,[10] Kohei Miyanishi,[11] Norimasa Ozaki,[3,12] Tatiana Pikuz,[3] Hirotaka Nakamura,[3] Keiichi Sueda,[11] Toshinori Yabuuchi,[11,13] Makina Yabashi,[11,13] Justin S. Wark,[1] Danae N. Polsin,[7] and Sam M. Vinko[1,14]

[1]*Department of Physics, Clarendon Laboratory, University of Oxford, Parks Road, Oxford OX1 3PU, United Kingdom*

[2]*Sorbonne Université, CNRS, Muséum National d'Histoire Naturelle, Institut de Minéralogie, de Physique des matériaux et de Cosmochimie, UMR7590 Paris, France*

[3]*Graduate School of Engineering, Osaka University, Suita, Osaka 565-0871, Japan*

[4]*Sorbonne Université, CNRS, Muséum National d'Histoire Naturelle, Institut de Minéralogie, de Physique des matériaux et de Cosmochimie, Institut Universitaire de France (IUF), UMR7590 Paris, France*

[5]*PIMM, Arts et Metiers Institute of Technology, CNRS, Cnam, HESAM University, 151 boulevard de l'Hôpital, 75013 Paris, France*

[6]*AWE, Aldermaston, Reading RG7 4PR, United Kingdom*

[7]*University of Rochester Laboratory for Laser Energetics, Rochester, New York 14623, USA*

[8]*SLAC National Accelerator Laboratory, 2575 Sand Hill Rd, Menlo Park, California 94025, USA*

[9]*European XFEL, GmbH, 22869 Schenefeld, Germany*

[10]*LULI, École Polytechnique, CNRS, CEA, UPMC, Palaiseau, France*

[11]*RIKEN SPring-8 Center, Hyogo 679-5148, Japan*

[12]*Institute of Laser Engineering, Osaka University, Suita, Osaka 565-0871, Japan*

[13]*Japan Synchrotron Radiation Research Institute, Hyogo 679-5198, Japan*

[14]*Central Laser Facility, STFC Rutherford Appleton Laboratory, Didcot OX11 0QX, United Kingdom*

(Received 21 June 2024; revised 10 January 2025; accepted 17 January 2025; published 29 January 2025)

We present measurements on Fe_2O_3 amorphization and melt under laser-driven shock compression up to 209(10) GPa via time-resolved *in situ* x-ray diffraction. At 122(3) GPa, a diffuse signal is observed indicating the presence of a noncrystalline phase. Structure factors have been extracted up to 182(6) GPa showing the presence of two well-defined peaks. A rapid change in the intensity ratio of the two peaks is identified between 145(12) and 151(12) GPa, indicative of a phase change. The noncrystalline diffuse scattering is consistent with shock amorphization of Fe_2O_3 between 122(3) and 145(12) GPa, followed by an amorphous-to-liquid transition above 151(12) GPa. Upon release, a noncrystalline phase is observed alongside crystalline α-Fe_2O_3. The extracted structure factor and pair distribution function of this release phase resemble those reported for Fe_2O_3 melt at ambient pressure.

DOI: 10.1103/PhysRevB.111.024209

I. INTRODUCTION

C rystalline and molten iron oxides are of particular interest for planetary and material sciences, given that the iron-rich outer core of the Earth contains up to 5% O, in addition to other light elements (Ni, S, Si, C, H) [1]. The study of iron oxide melts is thus important for the understanding of the Fe-O bonding environment within the outer core. Changes in Fe-O bonding in iron oxide melts have been proposed to be at the origin of a possible layering at the mid-Earth outer core [2], while seismological observations propose a stratification at the top of the Earth's outer core [3]. Layers within the outer core are expected to affect the geodynamo, making their characterization essential for precise geomagnetic modeling. The behavior of iron oxides under pressure has so far proven to be extremely rich, with the observation of new stoichiometry under pressure [4–6], and both electronic and structural phase transitions. In particular, under static compression, Fe_2O_3 undergoes a high-spin to low-spin, and a Mott insulator-to-metal, transition at around 50–60 GPa [7–10]. Five Fe_2O_3 phases have been reported with increasing pressure [11], all present along Fe_2O_3 Hugoniot based on temperature estimates from the SESAME 7440 equation of state [12]. However, a recent study claimed that Fe_2O_3 behaves differently under laser-driven shock compression: only one isostructural phase transition from α-Fe_2O_3 to α'-Fe_2O_3 is observed at

*Contact author: celine.crepisson@physics.ox.ac.uk

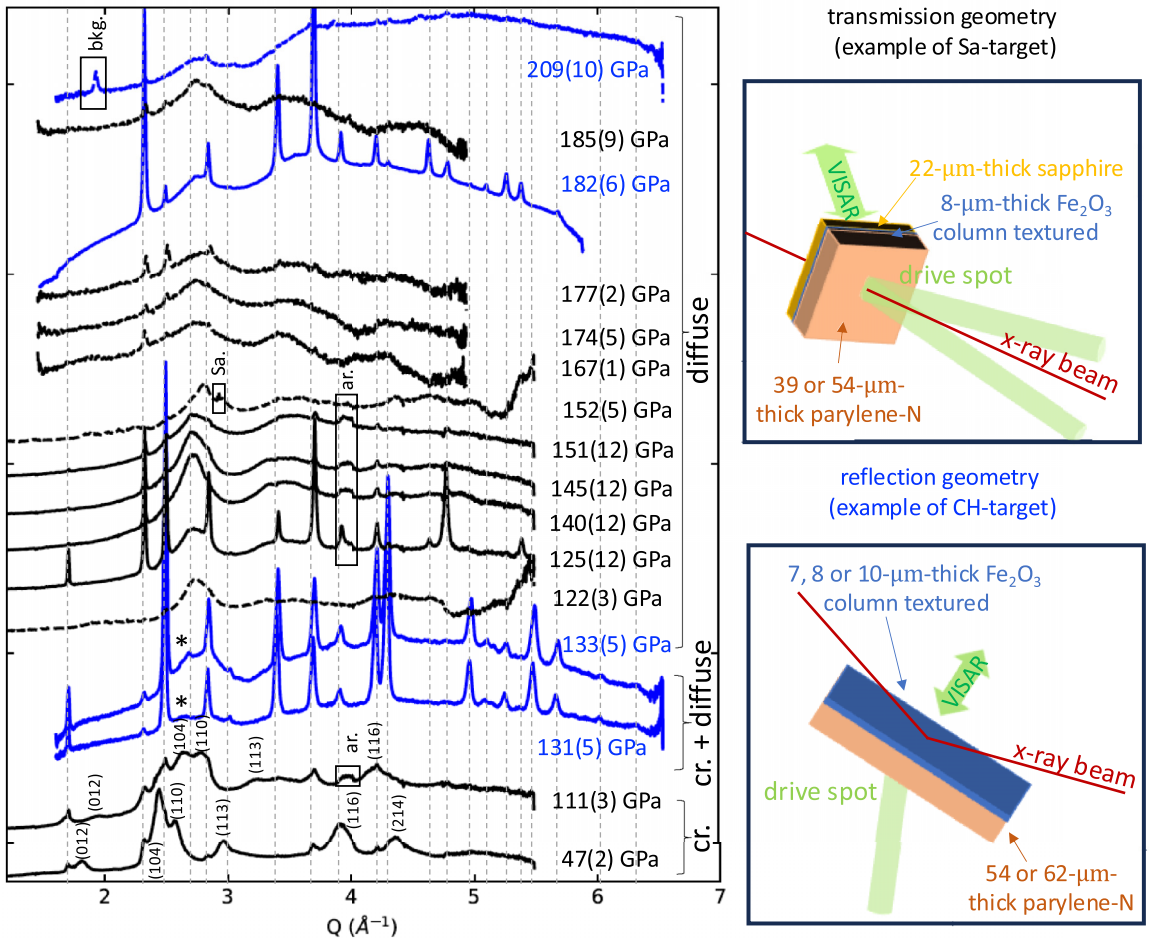

FIG. 1. X-ray diffraction measurements of Fe_2O_3 under shock compression. Azimuthally integrated XRD profiles under shock showing crystalline (cr.) Fe_2O_3 identified as α-Fe_2O_3 at 47(2) GPa and α'-Fe_2O_3 at 111(3) GPa with peak indexation reproduced from previous study [13]; appearance of diffuse feature at 131(5) and 133(5) GPa with remaining (104) peak of α'-Fe_2O_3 (indicated by *); and fully noncrystalline Fe_2O_3 from 122(3) to 209(10) GPa. Examples of 2D image plates are shown in Figs. S6 and S7. Solid lines correspond to CH target and dashed lines to Sa targets. Measurements acquired in transmission geometry are shown in black, and in reflection geometry in blue. Vertical dashed lines indicate the positions of α-Fe_2O_3 ambient peaks [19] present before breakout time. Spurious features in the data are indicated by: (Sa.) for a sapphire peak, (ar.) XRD integration artifacts, and (bkg.) for a background peak which was also observed on the same sample prior to the shock (Fig. S3). Only one detector could be used for data at 167, 174, 177, and 185 GPa due to technical reasons. Patterns are scaled for clarity.

~50–62 GPa, associated with a high-spin to low-spin transition, and possibly a further Mott transition [13]. The behavior of Fe_2O_3 above 116 GPa has, however, not been investigated yet under either dynamic or static compression, and its melting curve, as well as its melting point along the Hugoniot, remain unknown.

Here we report on *in situ* x-ray diffraction measurements of laser-driven shock compressed Fe_2O_3 between 122(3) GPa and 209(10) GPa. Our results indicate the appearance of a new noncrystalline phase, for which we compute the structure factor and pair distribution function for both data under shock and upon release. Temperatures along the Hugoniot are evaluated by DFT + U calculations, and are compared with the SESAME equation of state 7440 for Fe_2O_3. Our results show amorphization of Fe_2O_3 takes place for pressures up to 145(12) GPa, prior to melting above 151(12) GPa. Pressure-induced structural changes at the atomistic level for amorphous and molten phases are discussed.

II. METHODS

A. Experimental methods

As shown in Fig. 1, our primary experimental diagnostic is *in situ* x-ray diffraction (XRD) of laser-driven shock compressed samples, fielded in experiments at the Matter in Extreme Conditions (MEC) endstation at the Linac Coherent Light Source (LCLS) [14], and at the BL3 endstation at the Spring8 Angstrom Compact free electron LAser (SACLA) [15]. Both X-ray Free Electron Laser (XFEL) facilities operated in self-amplified spontaneous emission mode. We collected diffraction results in both transmission and reflection geometries.

For data in transmission, acquired at LCLS, two 527 nm laser beams arriving at 20° to the sample normal were focused on the target to a 300 µm maximum energy on the sample of 60 J. X rays at 7.09 keV (1.749Å) probed the target at an angle of 35° from the normal surface and a projected x-ray

spot size of 60 μm diameter in the center of the laser drive spot. 2D XRD images were recorded on 4 quadruple ePix10k detectors covered with a 50 μm thick Al filter and 125 μm thick plastic filter. Azimuthal integration of the 2D images includes polarization, solid angle and filter correction as well as self-attenuation from the target. For four data points (at 167, 174, 177, and 185 GPa), only one detector was used due to technical reasons and azimuthal integration of the 2D images for those data points was performed using Dioptas software [16] including polarization and solid angle correction.

For data in reflection, acquired at SACLA, one 532 nm laser beam arriving at 72° from the sample plane was focused on the target to a 260 μm diameter focal spot. Flat-top pulses had a duration of 5 ns and maximum energy on the sample was 13 J. X-rays at 9 or 9.98 keV (1.378 or 1.242 Å) probed the target at an angle of 18° from the surface plane, with a projected x-ray spot size of 40 μm diameter overlapping the laser drive spot. 2D XRD images were recorded on a single detector with no additional filter. Azimuthal integration of the 2D images was performed using Dioptas software [16] including polarization and solid angle correction.

In reflection geometry the x-rays probe 2-2.5 μm of Fe_2O_3 on the rear side (i.e., the side opposite to the laser interaction), whereas the entire sample (8 μm thick) is probed in transmission geometry, as shown in Fig. 1. Data in reflection are thus better resolved in time as only the last portion of the sample traversed by the shock is probed. Additionally, data in reflection are less affected by possible ablation-related preheat [17].

Two kinds of targets with different layer thicknesses were used, with each layer measured: CH targets, composed of a parylene-N ablator (54 and 62 μm thick) and a Fe_2O_3 layer (7, 8 and 10 μm thick); and Sa targets, composed of a parylene-N ablator (39 and 54 μm thick), a Fe_2O_3 layer (8 μm thick), and a sapphire window (22 μm thick). Further details on the layer thicknesses for the different measurements can be found in Sec. I of Ref. [18]. For all targets, polycrystalline column-textured Fe_2O_3 was created by physical vapor deposition and shown to correspond to α-Fe_2O_3 [19] by XRD, displayed in Fig. S3 [18]. A 200 nm Al coating was added on top of the parylene-N ablator to limit penetration of light in the parylene-N layer. No glue was used between the layers, which were deposited sequentially instead. The CH targets provide better XRD signal, as there is no attenuation or diffraction from the sapphire window, but the pressure determination is more reliable for Sa targets.

Velocity Interferometer System for any Reflector [20] (VISAR) was used to determine the breakout time, i.e., the moment when the shock leaves the Fe_2O_3 layer, and the velocity history. For the Sa targets the pressure was determined by using the particle velocity measured at the Fe_2O_3-sapphire interface, using impedance matching with the SESAME 7440 tables [12] for Fe_2O_3 and the SESAME 7411 tables [12] for sapphire. The apparent particle velocity measured in the sapphire was corrected to obtain the true particle velocity [21] following the same procedure as detailed in Ref. [13]. For the CH targets we could only measure the breakout time due to the loss of reflectivity of the sample. For these targets, the pressure was determined either by interpolating the breakout time versus pressure relationship obtained from the Sa targets, or via calibrated hydrodynamic simulations using the code MULTI [22], as further detailed in Figs. S4 and S5 [18]. During the experiment we defined the set delay which corresponds to the delay between the laser pulse (t = 0) and the XFEL probe. We determine the breakout time for each sample using VISAR analysis, t = 0 being known on the VISAR sweep window. The timing of the XFEL probe was adjusted throughout the experiment to probe the most homogeneous state, i.e., when most of the sample is under shock. Variation in ambient peak intensity observed in our data can be explained by the remaining unshocked material, whose volume varies with the probe timing shown in Table I [18]. For some Sa targets, the sample was probed up to 1 ns after breakout [at 122(3), 152(5), 185(9) and 209(10) GPa)] so that the entire sample is under shock as the shock is maintained up to 1.5 ns after breakout due to Fe_2O_3 and sapphire impedance matching (see Sec. VI of Ref. [18]). The remaining ambient peaks visible in those runs in Fig. 1 can be attributed to the halo around the x-ray beam present at the MEC beamline at LCLS, as detailed in Ref. [23].

B. Determination of structure factor and pair distribution function

The structure factor was calculated using the following equation:

$$S(Q) = A\frac{I(Q)}{f(Q)^2}, \tag{1}$$

with $I(Q)$ the intensity of the x-ray diffraction profile, $f(Q)$ the effective electronic form factor calculated using the atomic form factor [24] and A a normalization constant. We used the Ashcroft-Langreth formalism and calculated the Ashcroft-Langreth total structure factor as previously described [25]. The pair distribution function, $g(r)$, was then calculated for CH targets with maximal Q range between 5.5 and 5.9 $Å^{-1}$. Sa targets were discarded as their reliable Q range is limited to ~4 $Å^{-1}$ due to the sapphire signal. We calculated the Fourier transform of the structure factor to find

$$F(r) = \frac{2}{\pi}\int_0^{Q_{\max}} \sin(Qr)[S(Q) - S_\infty]\,dQ, \tag{2}$$

with r the radial interatomic distance and $Q_{\max}$ the highest available scattering momentum. The pair distribution function is then given by

$$g(r) = \frac{n(r)}{n_0} = 1 + \frac{F(r)}{4\pi n_0}, \tag{3}$$

with $n(r)$ the atomic density at a distance r from a given atom and n_0 the average atomic density at the experimental conditions. In our case, we determine the density at a given pressure using SESAME 7440 tables. To determine $g(r)$, we use an iterative process [26,27]. We minimize the background in $g(r)$ for the smallest interatomic distances ($r < r_{\min}$) where no real signal is expected:

$$r < r_{\min} \Rightarrow g(r) = 0 \Rightarrow F(r) = -4\pi r n_0,$$
$$\Delta F(r) = F(r) + 4\pi r n_0,$$

where $\Delta F(r)$ is the error on $F(r)$. $\Delta F(r)$ is then evaluated and removed from $F(r)$ to obtain the corresponding $g(r)$, from which a new $S(Q)$ can be calculated, and the cycle repeated.

C. Computational methods

Temperatures along the Fe_2O_3 Hugoniot were calculated using density functional theory with a Hubbard U parameter (DFT + U) [28–33]. Calculations were performed using the v7.2 Quantum-Espresso suite of codes [34,35]. Scalar-Relativistic ultrasoft pseudopotential (PP) [36] generated by PBEsol exchange-correlation functionals [37] were used for Fe and O. The effective Hubbard U parameter was used for the Fe-3d orbitals, with the initial occupations given by the PP. We used a kinetic energy cutoff of the plane-wave basis set of 100 Ry and an augmentation charge energy cutoff of 800 Ry. The calculations were carried out using a $12 \times 12 \times 12$ **k**-point grid. Our DFT + U calculations using $U = 5$ eV predict that at the ambient conditions, the energy band gap and the magnetic moment per iron atom are 2.075 eV and 4.41 μ_B, respectively. The corresponding experimental values are 2.14 eV [38] and 4.6 μ_B [39].

The equation of state (EOS) is obtained by performing DFT calculations at different densities in which the temperature effects were included using the quasiharmonic approximation [40]. The lattice dynamics and phonon spectra used in the quasiharmonic approximation were determined by density functional perturbation theory [40]. The phonon spectra were obtained using a $2 \times 2 \times 2$ **q**-point mesh. The Hugoniot pressure and temperature, P_H and T_H, are given by the Rankine-Hugoniot (RH) equation $\frac{1}{2}P_H[V_0 - V_H] = E_H - E_0$, where V_0 and E_0 are the volume and energy of the system at ambient conditions. The (RH) equation is solved using the EOS data by varying the temperature at a fixed volume until the RH condition is satisfied.

III. RESULTS

We first present the complete Fe_2O_3 diffraction dataset obtained in transmission and reflection geometries, and examine the series of pressure-induced changes to the structure factor between 47(2) and 209(10) GPa. A waterfall plot of the azimuthally integrated diffraction patterns is provided in Fig. 1. As has already been shown [13], Fe_2O_3 remains crystalline under shock compression up to 116 GPa. Above 131(5) GPa, we observed the onset of diffuse diffraction features for both the transmission and reflection geometries. The diffuse features at 2.7–2.8 $Å^{-1}$ are first observed at 122(3) GPa in transmission and at 131(5) GPa in reflection. The second diffuse feature at 3.4–3.6 $Å^{-1}$ becomes visible at 125(12) GPa in transmission geometry. These diffuse features persist up to the maximum pressure achieved in our experiments of 209(10) GPa.

In reflection geometry at 131(5) and 133(5) GPa, the diffuse feature is observed in coexistence with crystalline high pressure α'-Fe_2O_3 [13]. This is in contrast to measurements in transmission geometry, where no crystalline phase is visible from 122(3) GPa onwards. In reflection geometry only 2-2.5 μm on the rear side of the sample is probed, i.e., the remaining unshocked part of the sample and the region just behind the shock front. Kinetics of the amorphization or melting process could explain the remaining crystalline compressed phase just behind the shock front. Indeed, it has been shown for instance that the characteristic melting timescale in Ge is close to a few hundreds of picoseconds and can increase close to the melting point along the Hugoniot [41]. If the α'-Fe_2O_3 phase forms only as a thin layer just behind the shock front, its presence may appear as a faint peak in reflection geometry (Fig. 1) but could be obscured by the melt signal in transmission geometry. The reflection geometry enhances sensitivity to this region, as the volume just behind the shock front constitutes a larger portion of the probed volume compared with transmission geometry. This is in contrast to a situation where melt is present only as a faint signal, such as at the onset of melting. In such cases, previous studies have shown that it can be difficult to detect melt in transmission geometry as its XRD signal is too weak. However, it can be observed in reflection geometry, where it has a relatively larger contribution within the probed volume [42].

The ∼10 GPa difference observed between the pressures at which diffuse features appear and the crystalline phase disappears in transmission versus reflection geometries could be attributed to a preheat effect, which would induce a slightly higher temperature in transmission geometry at a given pressure. VISAR data show no detectable preheat, indicating that while preheat cannot be entirely ruled out, it remains low.

To better understand the structure of the noncrystalline phase and its evolution under pressure, we determined the structure factor $S(Q)$ and the pair distribution function $g(r)$ for samples without crystalline peaks. The baseline levels caused by emission from the ablation plasma was found on runs acquired on the same target and with the same experimental set-up (displayed in Fig. 1) that contained only solid crystalline diffraction. A scaled version of this background was then removed from all diffraction data before smoothing (further details for baseline removal can be found in Figs. S8 to S10). Our Q range for data under shock compression (∼5.5 $Å^{-1}$) leads to a limited resolution for $g(r)$ with a remaining background contribution below 1.5 Å. Therefore $g(r)$ cannot reliably be used to retrieve the structure of the noncrystalline phase, and will not be discussed in detail. This limited Q range, however, does not affect the determination of $S(Q)$ [26].

We can see in Fig. 2 that the structure factors of noncrystalline Fe_2O_3 under shock from 122(3) to 145(12) GPa present two peaks at 2.7–2.8 $Å^{-1}$ and 3.4–3.6 $Å^{-1}$. The structure factors presented here differ greatly from ambient pressure Fe_2O_3 melt [43], as can be seen in Fig. 2. To our knowledge, there is no existing data on amorphous or liquid Fe_2O_3 under pressure. Currently available data on molten FeO, available up to 70 GPa and 3500 K under static compression [44], show a very different structure factor than the one measured in our experiment. Above 145(12) GPa, significant further changes are observed. In terms of the structure factor, we observe both a slight shift of peak positions up to ∼+0.1 $Å^{-1}$ and a change in the intensity ratio. The peak at 3.5 $Å^{-1}$ becomes more prominent, and exceeds in intensity the first peak at around 2.7 $Å^{-1}$ at the highest pressures. Moreover, both peaks significantly broaden. These differences translate into $g(r)$ by a general shift toward shorter interatomic distances above 145(12) GPa. Between 151 and 182 GPa the second peak of the structure factor increases and shifts toward higher Q values. The rapid change observed above 145(12) GPa suggests the presence of a disorder-to-disorder phase transition.

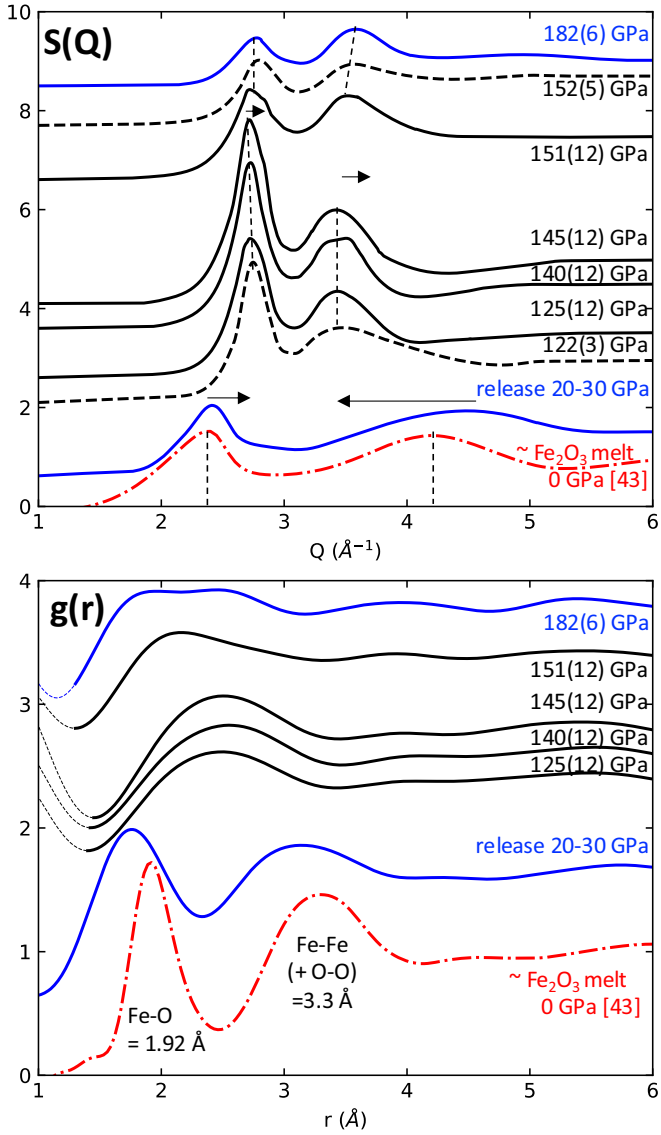

FIG. 2. Structure factor $S(Q)$ and $g(r)$ of Fe_2O_3. Structure factor for noncrystalline data points under shock and upon release. Data acquired in transmission geometry are shown in black, in reflection geometry in blue and ambient in red [43]. Dashed lines indicate Sa targets and solid lines CH targets. Data point upon release has a nonzero pressure as the reflection of the release wave off the parylene-N-Fe_2O_3 interface arrives on the free surface again exactly at the time when the sample is probed. Under shock, two peaks are seen in the structure factor, the position and intensity of which are strongly different from ambient melt and from noncrystalline phase observed upon release (see vertical dotted line and arrows for guidelines). Above 145(12) GPa, a slight shift of both peaks and an increase of the second peak intensity is observed. Despite limited resolution we can see a significant difference in $g(r)$ upon release and under shock as well as a general shift toward shorter interatomic distances above 145(12) GPa.

The evolution of the XRD signal of Fe_2O_3 upon release is shown in Fig. 3. We consider data acquired in reflection geometry on CH targets, shocked to pressures between 125(4) and 179(7) GPa, i.e., in the pressure range that shows a noncrystalline phase in Fig. 1. Data upon release were acquired

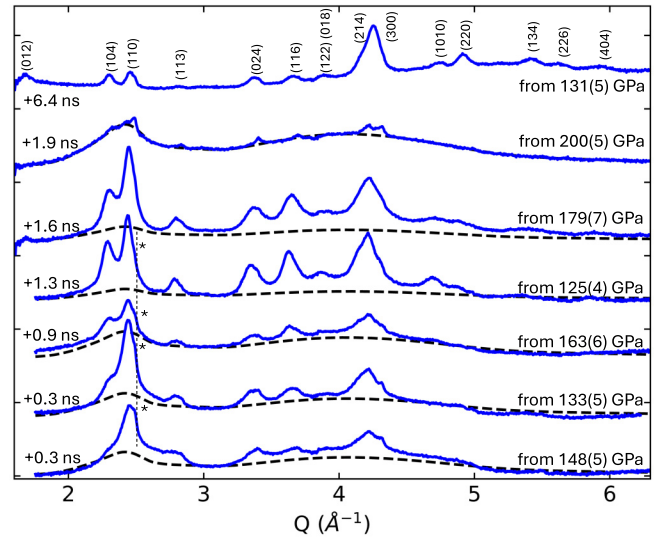

FIG. 3. X-ray diffraction measurements upon release. Azimuthally integrated x-ray diffraction profiles. Data are acquired in reflection geometry on CH target. Baseline has been subtracted to better assess the presence of a diffuse signal. The time after the shock leaves the target is indicated on the left. Crystalline peaks are seen in coexistence with diffuse features around 2.4 $Å^{-1}$ and 4.5 $Å^{-1}$ up to 0.9 ns. Very few crystalline peaks are observed for one release at 1.9 ns after breakout time after shock corresponding to 200(5) GPa: at this timing, the release wave originating at the free-surface of the Fe_2O_3 layer reflects off the parylene-N-Fe_2O_3 interface and reaches the free surface again (see Fig. S11). Diffuse signal observed at 1.9 ns after breakout time is shown as black dashed curve and adjusted by a multiplicative factor for all data up to 1.9 ns, showing the clear presence of a similar diffuse signal for release runs at 0.3 and 0.9 ns and later in time at 1.9 ns after breakout time. Peaks of α-Fe_2O_3 are indexed [19]. The (110) peak of α'-Fe_2O_3 indicated by *, is observed until 1.3 ns, proving that the sample is still releasing up to this timing.

on similar CH targets as those probed under shock in the same experiment (as detailed in Sec. I of Ref. [18]), i.e., 7 μm of Fe_2O_3 deposited on top of 54.3 μm parylene-N. We observe a diffuse signal at 2.4 and 4.5 $Å^{-1}$ in coexistence with crystalline Fe_2O_3, up to approximately 0.9 ns after breakout time. Purely crystalline Fe_2O_3 is mostly observed beyond 0.9 ns. The α-Fe_2O_3 phase is mostly present in coexistence with α'-Fe_2O_3, whose (110) peak is visible up to 1.3 ns after breakout time. A case of particular interest is at 1.9 ns after breakout, after a shock at 200(5) GPa, where the release wave originating at the free-surface of the Fe_2O_3 layer reflects off the parylene-N-Fe_2O_3 interface, and reaches the free surface again. The XRD pattern taken at this time shows a loss of crystalline peaks and a noncrystalline signal. The diffuse signal is shown as a black dashed curve and adjusted by a multiplicative factor for all data up to 1.9 ns. It shows the clear presence of a similar diffuse signal in Fig. 3 for release runs at 0.3, 0.9, and 1.9 ns after breakout time, while the diffuse signal is barely visible for release runs at 1.3 and 1.6 ns. The high proportion of the noncrystalline phase at this data point may be related to the elevated pressure under shock, which exceeds that of other release data points and suggests a distinct release path. However, fully understanding the unloading history is

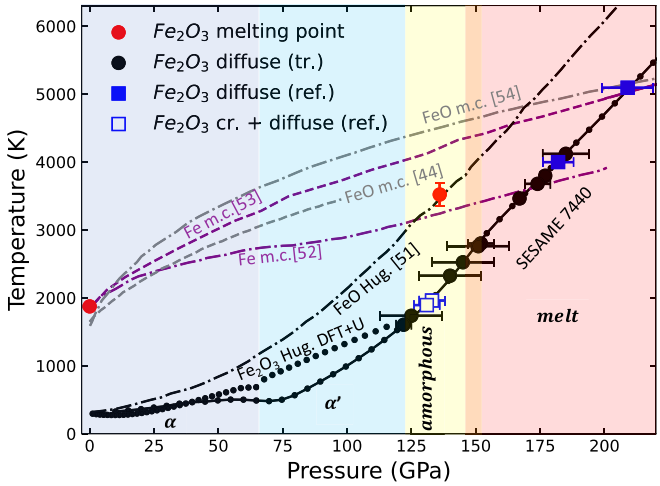

FIG. 4. Temperature-pressure diagram of Fe_2O_3 under shock. We represent our data points acquired in transmission (tr.) or reflection (ref.) geometries with diffuse features and in some cases remaining crystals (cr.) under shock. The temperature was not measured independently in the experiment, and the data are shown following the predicted temperatures from the SESAME 7440 hugoniot. Results of DFT + U calculations, for α-Fe_2O_3 (0 to 65 GPa) and α'-Fe_2O_3 (65 to 115 GPa) phases, based on previous shock data [13]) are shown as black dotted curve. Phases observed along Fe_2O_3 Hugoniot under shock compression are summarized: α-Fe_2O_3 stable up to approximately 50 GPa and α'-Fe_2O_3 phases, observed alone, above 80 GPa [13], amorphous phase from 122(3) to 145(12) GPa and melt from 151(12) GPa. Colours are used as a guide to distinguish phases along the Hugoniot and do not infer phases off-Hugoniot. The melting point at 0 GPa is taken from Ref. [49] and the assumed melting point at 136 GPa from Ref. [50]. For comparison, we also show the FeO Hugoniot (Hug.) [51], and the melting curves (m.c.) of Fe [52,53] and FeO [44,54].

challenging due to the complex range of phenomena occurring during release at this later stage, which are not captured in our hydrodynamic simulations. The noncrystalline signal, similar to earlier release data points (up to 0.9 ns after breakout time) where no reflection of release wave yet occurred, can more easily be extracted on this particular data point to get $S(Q)$ and $g(r)$, displayed in Fig. 2. We note that the extracted $S(Q)$ and $g(r)$ differ significantly from the data under shock, but are similar to data taken on molten Fe_2O_3 at ambient pressure [43], with a slight shift linked to pressure arising from the reflection of the release wave as previously described. We have thus observed a disordered phase, the structure of which resembles ambient, molten Fe_2O_3 [43], recrystallizing in time.

Our DFT + U calculations are shown on the temperature-pressure diagram in Fig. 4. Good agreement is observed between the SESAME 7440 and the DFT + U calculations between 0 and 65 GPa, i.e., where the α-Fe_2O_3 phase is stable. A change in slope is observed at 65 GPa, linked to the isostructural phase transition reported under shock [13]. For α'-Fe_2O_3, discrepancies of around 250–440 K are observed between the DFT + U calculations and the SESAME 7440 predictions from 70 to 110 GPa. These discrepancies can be attributed to the assumption of an α'-Fe_2O_3 phase for the DFT + U calculations, while SESAME 7440 was computed before any phase identification of Fe_2O_3 under shock [12] and uses a different methodology [45,46]. This illustrates the importance of developing Hugoniot calculations based on phases experimentally reported along the Hugoniot. Nevertheless, DFT + U calculations indicate a temperature of 1600 K at 115 GPa compared with 1400 K from SESAME 7440, so broadly similar at this pressure despite differing initial assumptions and calculation methods.

IV. DISCUSSION

Temperature measurements during shock compression experiments remain scarce. Moreover, shock temperature cannot be directly extracted from the Rankine-Hugoniot relations and approximations are needed to evaluate temperature along the Hugoniot [47,48]. For these reasons there is still a large uncertainty on temperature estimates along the Hugoniot of various materials. Temperatures along the Fe_2O_3 Hugoniot are only known from theoretical calculations or equation of state tables [45] such as SESAME 7440, shown in Fig. 4. However, because we know that under shock compression the phases are different to those observed statically [13], we have performed DFT + U calculations using the phases directly observed under shock up to 116 GPa to determine the temperature along Fe_2O_3 Hugoniot. This provides an alternative method, based on our most recent results, to constrain the temperature range at 115 GPa along the Fe_2O_3 Hugoniot, prior to the phase transition from the α'-Fe_2O_3 phase to the noncrystalline phase reported here. Overall, temperatures are seen to remain below 1600 K up to 115 GPa, and while there are some discrepancies between our calculations and the SESAME 7440 tables, the two do not differ substantially. We use this observation to guide our temperature estimates at higher pressures, where the system enters a disordered (amorphous or molten) phase above 122(3) GPa. There are no experimental measurements or theoretical predictions for the Hugoniot temperatures at these higher pressures, and the *ab initio* calculations become increasingly challenging to perform and validate. We thus revert to using the SESAME 7440 tables for data between 122(3) and 209(10) GPa, but note that this introduces a fundamental limitation to the accuracy within which the temperature can be estimated.

At ambient pressure Fe_2O_3 melts at 1873 K [49]. Although the melting curve of Fe_2O_3 has not been measured to date, a melting temperature of 3350–3690 K at 136 GPa was estimated for η-Fe_2O_3 from first-principles molecular dynamic melting temperature calculations for FeO_2H_x [50] assuming a linear relationship between the melting temperature and the oxygen content for a FeO_x system. Fe_2O_3 could thus, conceivably, melt at a lower temperature than FeO under pressure. Temperatures for data acquired at 122-133 GPa remain below the ambient pressure melting point of Fe_2O_3. We consequently attribute the diffuse features observed at this pressure to an amorphization of Fe_2O_3 under shock, although the possibility of a negative melting curve for Fe_2O_3 [55], which could explain the presence of a melt at 122–133 GPa along the shock Hugoniot, cannot be entirely discarded.

Solid state amorphization under shock compression has been reported on a wide range of materials [56,57] including silica [58] and silicates such as plagioclase [59], enstatite [60],

or olivine [61–63], as well as in covalently bonded solids such as Ge, Si, SiC, and B_4C [64]. Amorphization has been shown to be favored by compression, shear and high strain-rates, as present during shock compression. While it remains debated why and how a material becomes amorphous, amorphization is commonly linked to deformation mechanisms. It is seen either as the final step of plastic deformation or as an alternative deformation mechanism in competition with other types of deformations [56,57]. DFT + U calculations were performed to determine the bulk and Young moduli of α'-Fe_2O_3 phase at 120 GPa and assess its stability with respect to the applied shear stress. The elastic constants tensor is used to obtain the bulk modulus B, Young modulus Y, shear modulus G, and Poisson ratio n. We first validated our DFT + U simulations by verifying the accuracy of the derived B, Y, G and n, for the ambient α-Fe_2O_3 phase, which in the experiment (versus in the simulation) take values of 203(4) GPa [65,66] (versus 212 GPa), 220 GPa [67] (versus 241 GPa), 101(9) GPa [65] (versus 92 GPa), and 0.31 [65] (versus 0.31), respectively. We performed the same calculations for the α'-Fe_2O_3 phase at 120 GPa, and it was found that both the shear modulus and Young modulus are negative. The negative shear modulus suggests that the α' crystal structure cannot sustain the applied shear stress, leading to a deformation or structural rearrangement. This is consistent with the observed destabilization of the α'-Fe_2O_3 phase, transforming into an amorphous phase at 122(3) GPa. We thus conclude that above 122(3) GPa, amorphous Fe_2O_3 is kinetically favourable compared with other crystalline phases, and to further deformation of α'-Fe_2O_3, whose shear and Young moduli are found to be negative at this pressure.

The change in the peak intensity ratio observed between 145(12) GPa and 151(12) GPa translates into $g(r)$ by a general shift toward shorter interatomic distances above 145(12) GPa, as shown in Fig. 2. An increase in the intensity of the second peak of the structure factor under pressure is frequent in silicate glasses and melts, and is attributed to the gradual transition from fourfold to sixfold coordinated Si [59,63,68,69]. Nevertheless, noncrystalline Fe_2O_3 structure is unlikely to be comparable with glass and melt silicate structures under pressure, and measurements at higher Q range will be needed to uncover the Fe-O and Fe-Fe interatomic distances and coordination numbers to fully interpret this observation. In our case, the peak ratio intensity rapidly changes within 6 GPa (from 145(12) to 151(12) GPa) while both peaks broaden. This can be either interpreted as a melting of Fe_2O_3, or a rapid transition from amorphous Fe_2O_3 to another amorphous phase. The change observed here, within a few GPa, seems to be in better agreement with the melting of Fe_2O_3. Indeed, changes observed so far in amorphous phases under shock are gradual, such as observed for amorphous plagioclase [59]. Amorphous phases are also seen to span large pressure ranges with no structural variation under shock compression, as shown for enstatite [60], but also as reported here in Fig. 2 where the structure factors remain unchanged between 122(3) and 145(12) GPa. The subsequent change observed from 145(12) to 151(12) GPa can be related to the rapid structural evolution of the melt, whose structure factor is also seen to evolve significantly as the pressure is increased further. The melting of Fe_2O_3 at 151 GPa along the Hugoniot would thus indicate a relatively low melting temperature around 2500 K.

Previous laser shock data has shown that the phase transition observed along the Fe_2O_3 Hugoniot between 140 and 300 GPa is accompanied by an increase in density and thus a decrease in volume [55]. If the observed transition is associated to melting based on the present results, this will indicate a negative Clapeyron slope for the Fe_2O_3 melting curve. Then, the amorphization observed prior to melting could be explained by the Fe_2O_3 Hugoniot crossing the metastable extension of the Fe_2O_3 melting curve at around 122(3) GPa, a phenomenon already reported for quartz [70]. We note, however, that amorphization prior to melting under shock is also observed for enstatite [60] and olivine [63], whose melting curves present a positive slope at the investigated pressures. No discontinuity is observed along the Fe_2O_3 Hugoniot between 100 and 140 GPa [55,71,72] which could indicate that amorphous Fe_2O_3 has a density close to α'-Fe_2O_3 observed up to 116 GPa [13].

As we show in Fig. 2, the structure factor and pair distribution function of the noncrystalline release phase observed at 1.9 ns after breakout is similar to that of liquid Fe_2O_3 at ambient pressure [43], apart from a slight shift of −0.16 Å, which we attribute to the pressure linked with the release wave originating at the free surface of the Fe_2O_3 layer reflecting off the parylene-N-Fe_2O_3 interface and reaching the free surface exactly when the sample is probed. While we cannot take into account the full variety of processes occurring upon release in our hydrodynamic simulations, we are able to estimate the pressure of the system based on the observed bond length decrease. Assuming an isotropic compression, we estimate the pressure based on the Fe-O or Fe-Fe bond lengths upon release (d), the bond lengths at ambient pressure [43] (d_0), and the adiabatic modulus (K) of liquid FeO [73] (as no data is available for liquid or amorphous Fe_2O_3), as given by

$$P = -K \ln\left(\frac{d^3}{d_0^3}\right). \tag{4}$$

We find a pressure of ∼30 and 20 GPa from the Fe-O and Fe-Fe bond length decreases, respectively. The diffuse features observed upon release decrease in intensity up to 0.9 ns after breakout time after shock of 125(4) to 179(7) GPa. In contrast, features from the α'-Fe_2O_3 phase persist for longer, indicating that the sample is still releasing up to around 1.3 ns, as shown in Fig. 3. These observations could indicate either the presence of a melt recrystallizing in time, explaining the similarity of the noncrystalline release phase with liquid from α-Fe_2O_3 at ambient pressure [43], or the relaxation and the recrystallization of the amorphous phase with a structure similar to the corresponding liquid at ambient pressure. Similar results and observations were reported for forsterite upon release [62]. We note that for a release after a higher pressure shock of 200(5) GPa the noncrystalline phase is dominant at 1.9 ns after breakout in one case, where the reflection of a release wave off the parylene-N-Fe_2O_3 interface reaches the Fe_2O_3 layer. This implies a need to consider the full unloading history of the sample to understand the entire behavior of Fe_2O_3 upon release through timing.

V. CONCLUSION

It has been recently claimed that shock-compressed Fe_2O_3 does not experience any of the phase transitions reported by static compression up to 116 GPa, but instead undergoes an isostructural transition (from α- to α'-Fe_2O_3) at 50-62 GPa [13]. In the present study we show that from 122–131 GPa up to 145(12) GPa, amorphization is preferred to either deformed α'-Fe_2O_3 or to other potential phase transitions. This is similar to previously reported results for covalently- or partially-covalently-bonded solids [64]. Between 145(12) and 151(12) GPa we observe a rapid change in the peak intensity ratio in the structure factor. We attribute this to the appearance of Fe_2O_3 melt, which rapidly evolves under pressure. Further experiments at higher photon energy should make it possible to access higher Q range and thoroughly explain these observations in terms of structural evolution of amorphous and molten phases.

ACKNOWLEDGMENTS

Use of the Linac Coherent Light Source (LCLS), SLAC National Accelerator Laboratory, is supported by the U.S. Department of Energy, Office of Science, Office of Basic Energy Sciences under Contract No. DE-AC02-76SF00515. Part of the experiment was performed at BL3 of SACLA with the approval of the Japan Synchrotron Radiation Research Institute (JASRI) (Proposals No. 2021A8643 and No. 2023A8061), in combination with the high-power nanosecond laser of the Institute of Laser Engineering, Osaka University. A.A., H.N., T.P., and N.O. were supported by grants from Japan Society for the Promotion of Science (JSPS) KAKENHI (Grants No. 22KF0243, No. 20H00139, No. 22K18702, and No. 23K20038), JSPS Core-to-Core program (Grant No. JPJSCCA20230003), and MEXT Q-LEAP (Grant No. JP-MXS0118067246). This project has received funding from the European Research Council (ERC) under the European Union's Horizon 2020 research and innovation program (ERC PLANETDIVE Grant Agreement No. 670787). This material is based upon work supported by the Department of Energy [National Nuclear Security Administration] University of Rochester "National Inertial Confinement Fusion Program" under Award No. DE-NA0004144. C.C., P.G.H., S.A., J.S.W and S.M.V. acknowledge support from the UK EPSRC under Grants No. EP/P015794/1, No. EP/X031624/1, and No. EP/W010097/1. T.G. acknowledges support from AWE via the Oxford Centre for High Energy Density Science (OxCHEDS). T.C. and S.M.V. acknowledge support from the Royal Society. A.F. acknowledges support from the STFC UK Hub for the Physical Sciences on XFELs. We thank the microscopy, x-ray diffraction and PVD platforms at IMPMC for support in producing and characterizing the Fe_2O_3 samples.

[1] K. Hirose, B. Wood, and L. Vočadlo, Light elements in the earth's core, Nat. Rev. Earth Environ. **2**, 645 (2021).

[2] H. Ozawa, F. Takahashi, K. Hirose, Y. Ohishi, and N. Hirao, Phase transition of feo and stratification in earth's outer core, Science **334**, 792 (2011).

[3] R. van Tent, A. Deuss, S. Kaneshima, and C. Thomas, The signal of outermost-core stratification in body-wave and normal-mode data, Geophys. J. Int. **223**, 1338 (2020).

[4] B. Lavina, P. Dera, E. Kim, Y. Meng, R. T. Downs, P. F. Weck, S. R. Sutton, and Y. Zhao, Discovery of the recoverable high-pressure iron oxide Fe_4O_5, Proc. Natl. Acad. Sci. USA **108**, 17281 (2011).

[5] B. Lavina and Y. Meng, Unraveling the complexity of iron oxides at high pressure and temperature: Synthesis of Fe_5O_6, Sci. Adv. **1**, e1400260 (2015).

[6] R. Sinmyo, E. Bykova, S. V. Ovsyannikov, C. McCammon, I. Kupenko, L. Ismailova, and L. Dubrovinsky, Discovery of Fe_7O_9: a new iron oxide with a complex monoclinic structure, Sci. Rep. **6**, 32852 (2016).

[7] M. P. Pasternak, G. K. Rozenberg, G. Y. Machavariani, O. Naaman, R. D. Taylor, and R. Jeanloz, Breakdown of the mott-hubbard state in Fe_2O_3: A first-order insulator-metal transition with collapse of magnetism at 50 GPa, Phys. Rev. Lett. **82**, 4663 (1999).

[8] E. Greenberg, I. Leonov, S. Layek, Z. Konopkova, M. P. Pasternak, L. Dubrovinsky, R. Jeanloz, I. A. Abrikosov, and G. K. Rozenberg, Pressure-induced site-selective mott insulator-metal transition in Fe_2O_3, Phys. Rev. X **8**, 031059 (2018).

[9] J. Badro, G. Fiquet, V. V. Struzhkin, M. Somayazulu, H.-K. Mao, G. Shen, and T. LeBihan, Nature of the high-pressure transition in Fe_2O_3 hematite, Phys. Rev. Lett. **89**, 205504 (2002).

[10] A. Sanson, I. Kantor, V. Cerantola, T. Irifune, A. Carnera, and S. Pascarelli, Local structure and spin transition in Fe_2O_3 hematite at high-Pressure, Phys. Rev. B **94**, 014112 (2016).

[11] E. Bykova, L. Dubrovinsky, N. Dubrovinskaia, M. Bykov, C. McCammon, S. Ovsyannikov, H.-P. Liermann, I. Kupenko, A. Chumakov, R. Ruffer, M. Hanfland, and V. Prakapenka, Structural complexity of simple Fe_2O_3 at high pressures and temperatures, Nat. Commun. **7**, 10661 (2016).

[12] J. Barnes and S. Lyon, SESAME: The Los Alamos Scientific Laboratory, Equation of State Database, Report No. LA-UR-92-3407 (unpublished).

[13] A. Amouretti, C. Crepisson, S. Azadi, D. Cabaret, T. Campbell, D. A. Chin, B. Colin, G. R. Collins, L. Crandall, G. Fiquet, A. Forte, T. Gawne, F. Guyot, P. Heighway, H. Lee, D. McGonegle, B. Nagler, J. Pintor, D. Polsin, G. Rousse *et al.*, Phase transitions of Fe_2O_3 under laser shock compression, arXiv:2402.18432.

[14] B. Nagler, B. Arnold, G. Bouchard, R. F. Boyce, R. M. Boyce, A. Callen, M. Campell, R. Curiel, E. Galtier, J. Garofoli, E. Granados, J. Hastings, G. Hays, P. Heimann, R. W. Lee, D. Milathianaki, L. Plummer, A. Schropp, A. Wallace, M. Welch *et al.*, The matter in extreme conditions instrument at the linac coherent light source, J. Synchrotron Radiat. **22**, 520 (2015).

[15] M. Yabashi, H. Tanaka, and T. Ishikawa, Overview of the SACLA facility, J. Synchrotron Radiat. **22**, 477 (2015).

[16] C. Prescher and V. B. Prakapenka, Dioptas: a program for reduction of two-dimensional x-ray diffraction data and data exploration, High Press. Res. **35**, 223 (2015).

[17] K. Falk, Experimental methods for warm dense matter research, High Power Laser Sci. Eng. **6**, e59 (2018).

[18] See Supplemental material at http://link.aps.org/supplemental/10.1103/PhysRevB.111.024209 for experimental details and targets, estimates of pressure based on VISAR analysis and hydrodynamic simulations, example of 2D diffraction images, baseline subtraction for azimuthally integrated XRD profiles and tables summarizing experimental data points and DFT+U results, and which includes Refs. [74,75].

[19] R. L. Blake, R. E. Hessevick, T. Zoltai, and L. W. Finger, Refinement of the Hematite structure, Am. Mineral. **51**, 123 (1966).

[20] L. M. Barker and R. E. Hollenbach, Laser interferometer for measuring high velocities of any reflecting surface, J. Appl. Phys. **43**, 4669 (1972).

[21] X. Cao, Y. Wang, X. Li, L. Xu, L. Liu, Y. Yu, R. Qin, W. Zhu, S. Tang, L. He, C. Meng, B. Zhang, and X. Peng, Refractive index and phase transformation of sapphire under shock pressures up to 210 GPa, J. Appl. Phys. **121**, 115903 (2017).

[22] R. Ramis, J. M. ter Vehn, and J. Ramírez, Multi2d – a computer code for two-dimensional radiation hydrodynamics, Comput. Phys. Commun. **180**, 977 (2009).

[23] A. Descamps, B. K. Ofori-Okai1, O. Bistoni, Z. Chen, E. Cunningham, L. B. Fletcher, N. J. Hartley, J. B. Hastings, D. Khaghani, M. Mo, B. Nagler, V. Recoules, R. Redmer, M. Schörner, D. G. Senesky, P. Sun, H.-E. Tsai, T. G. White, S. H. Glenzer, and E. E. McBride, Evidence for phonon hardening in laser-excited gold using x-ray diffraction at a hard x-ray free electron laser, Sci. Adv. **10**, eadh5272 (2024).

[24] F. Hadju, Revised parameters of the analytic fits for coherent and incoherent scattered x-ray intensities of the first 36 atoms, Acta Crystallogr. Sect. A **A28**, 250 (1972).

[25] B. J. Heinen and J. W. E. Drewitt, Liquiddiffract: Software for liquid total scattering analysis, Phys. Chem. Miner. **49**, 9 (2022).

[26] J. H. Eggert, G. Weck, P. Loubeyre, and M. Mezouar, Quantitative structure factor and density measurements of high-pressure fluids in diamond anvil cells by x-ray diffraction: Argon and water, Phys. Rev. B **65**, 174105 (2002).

[27] C. Sanloup, F. Guyot, P. Gillet, G. Fiquet, R. J. Hemley, M. Mezouar, and I. Martinez, Structural changes in liquid Fe at high pressures and high temperatures from synchrotron x-ray diffraction, Europhys. Lett. **52**, 151 (2000).

[28] P. Hohenberg and W. Kohn, Inhomogeneous electron gas, Phys. Rev. **136**, B864 (1964).

[29] W. Kohn and L. J. Sham, Self-consistent equations including exchange and correlation effects, Phys. Rev. **140**, A1133 (1965).

[30] V. I. Anisimov, J. Zaanen, and O. K. Andersen, Band theory and mott insulators: Hubbard U instead of stoner I, Phys. Rev. B **44**, 943 (1991).

[31] A. I. Liechtenstein, V. I. Anisimov, and J. Zaanen, Density-functional theory and strong interactions: Orbital ordering in Mott-Hubbard insulators, Phys. Rev. B **52**, R5467 (1995).

[32] S. L. Dudarev, G. A. Botton, S. Y. Savrasov, C. J. Humphreys, and A. P. Sutton, Electron-energy-loss spectra and the structural stability of nickel oxide: An LSDA+U study, Phys. Rev. B **57**, 1505 (1998).

[33] M. Cococcioni and S. de Gironcoli, Linear response approach to the calculation of the effective interaction parameters in the LDA+U method, Phys. Rev. B **71**, 035105 (2005).

[34] P. Giannozzi, S. Baroni,N. Bonini, M. Calandra, R. Car, C. Cavazzoni, D. Ceresoli, G. L. Chiarotti, M. Cococcioni, I. Dabo, A. Dal Corso, S. Fabris, G. Fratesi, S. de Gironcoli, R. Gebauer, U. Gerstmann, C. Gougoussis, A. Kokalj, M. Lazzeri, L. Martin-Samos *et al.*, QUANTUM ESPRESSO: A modular and open-source software project for quantum simulations of materials, J. Phys.: Condens. Matter **21**, 395502 (2009).

[35] P. Giannozzi, O. Andreussi, T. Brumme, O. Bunau, M. Buongiorno Nardelli, M. Calandra, R. Car, C. Cavazzoni, D. Ceresoli, M. Cococcioni, N. Colonna, I. Carnimeo, A. Dal Corso, S. de Gironcoli, P. Delugas, R. A. DiStasio, Jr., A. Ferretti, A. Floris, G. Fratesi, G. Fugallo *et al.*, Advanced capabilities for materials modelling with QUANTUM ESPRESSO, J. Phys.: Condens. Matter **29**, 465901 (2017).

[36] A. Dal Corso, Pseudopotentials periodic table: From H to Pu, Comput. Mater. Sci. **95**, 337 (2014).

[37] J. P. Perdew, A. Ruzsinszky, G. I. Csonka, O. A. Vydrov, G. E. Scuseria, L. A. Constantin, X. Zhou, and K. Burke, Restoring the density-gradient expansion for exchange in solids and surfaces, Phys. Rev. Lett. **100**, 136406 (2008).

[38] D. Benjelloun, J.-P. Bonnet, J.-P. Doumerc, J.-C. Launay, M. Onillon, and P. Hagenmuller, Anisotropie des proprietes electriques de l'oxyde de fer Fe_2O_3-α-, Mater. Chem. Phys. **10**, 503 (1984).

[39] J. M. D. Coey and G. A. Sawatzky, A study of hyperfine interactions in the system $(Fe_1\text{-}xRhx)_2O_3$ using the mossbauer effect (bonding parameters), J. Phys. C **4**, 2386 (1971).

[40] S. Baroni, S. de Gironcoli, A. Dal Corso, and P. Giannozzi, Phonons and related crystal properties from density-functional perturbation theory, Rev. Mod. Phys. **73**, 515 (2001).

[41] P. Renganathan, S. M. Sharma, S. J. Turneaure, and Y. M. Gupta, Real-time (nanoseconds) determination of liquid phase growth during shock-induced melting, Sci. Adv. **9**, eade5745 (2023).

[42] E. E. McBride, A. Krygier, A. Ehnes, E. Galtier, M. Harmand, Z. Konôpková, H. J. Lee, H.-P. Liermann, B. Nagler, A. Pelka, M. Rödel, A. Schropp, R. F. Smith, C. Spindloe, D. Swift, F. Tavella, S. Toleikis, T. Tschentscher, J. S. Wark, and A. Higginbotham, Phase transition lowering in dynamically compressed silicon, Nat. Phys. **15**, 89 (2019).

[43] C. Shi, O. L. G. Alderman, A. Tamalonis, R. Weber, J. You, and C. J. Benmore, Redox-structure dependence of molten iron oxides, Commun. Mater. **1**, 80 (2020).

[44] G. Morard, D. Antonangeli, J. Bouchet, A. Rivoldini, S. Boccato, F. Miozzi, E. Boulard, H. Bureau, M. Mezouar, C. Prescher, S. Chariton, and E. Greenberg, Structural and Electronic Transitions in Liquid FeO Under High Pressure, J. Geophys. Res. Solid Earth **127**, e2022JB025117 (2022).

[45] P. Kalita, K. R. Cochrane, M. D. Knudson, T. Ao, C. Blada, J. Jackson, J. Gluth, H. Hanshaw, E. Scoglietti, and S. D. Crockett, Ti-6Al-4V to over 1.2 TPa: Shock Hugoniot experiments, ab

initio calculations, and a broad-range multiphase equation of state, Phys. Rev. B **107**, 094101 (2023).

[46] J. McHardy, An introduction to the theory and use of SESAME equation of state, report LA-14503 from Los Alamos National Laboratory (2018), https://www.osti.gov/servlets/purl/1487368/.

[47] S. Raikes and T. Ahrens, Post-shock temperatures in minerals, Geophys. J. Int. **58**, 717 (1979).

[48] T. G. Sharp, P. S. DeCarli, R. P. Binzel, R. M. Walker, and A. G. W. Cameron, Shock effects in meteorites, in *Meteorites and the Early Solar System II*, edited by D. S. Lauretta and H. Y. McSween (University of Arizona Press, 2006), pp. 653–78.

[49] A. K. Biswas, *Principles of Blast Furnace Ironmaking : Theory and Practice* (Cootha Publishing House Brisbane, Australia, 1981).

[50] J. Deng, B. B. Karki, D. B. Ghosh, and K. K. M. Lee, First-Principles study of FeO_2H_x solid and Melt system at high pressures: implications for ultralow-velocity zones, J. Geophys. Res.: Solid Earth **124**, 4566 (2019).

[51] R. Jeanloz and T. J. Ahrens, Equations of state of FeO and CaO, Geophys. J. Int. **62**, 505 (1980).

[52] R. Boehler, Temperatures in the Earth's core from melting-point measurements of iron at high static pressures, Nature (London) **363**, 534 (1993).

[53] S. Anzellini, A. Dewaele, M. Mezouar, P. Loubeyre, and G. Morard, Melting of iron at earth's inner core boundary based on fast x-ray diffraction, Science **340**, 464 (2013).

[54] V. V. Dobrosavljevic, D. Zhang, W. Sturhahn, S. Chariton, V. B. Prakapenka, J. Zhao, T. S. Toellner, O. S. Pardo, and J. M. Jackson, Melting and defect transitions in FeO up to pressures of Earth's core-mantle boundary, Nat. Commun. **14**, 7336 (2023).

[55] A. Amouretti, M. Harmand, B. Albertazzi, A. Boury, A. Benuzzi-Mounaix, D. A. Chin, F. Guyot, M. Koenig, T. Vinci, and G. Fiquet, Laser-driven shock compression and equation of state of Fe_2O_3 up to 700 GPa, arXiv:2405.08350.

[56] H. Idrissi, P. Carrez, and P. Cordier, On amorphization as a deformation mechanism under high stresses, Curr. Opin. Solid State Mater. Sci. **26**, 100976 (2022).

[57] B. Li, A. Li, S. Zhao, and M. Meyers, Amorphization by mechanical deformation, Mater Sci Eng R: Rep. **149**, 100673 (2022).

[58] S. J. Tracy, S. J. Turneaure, and T. S. Duffy, In situ X-Ray Diffraction of Shock-Compressed Fused Silica, Phys. Rev. Lett. **120**, 135702 (2018).

[59] A. E. Gleason, S. Park, D. R. Rittman, A. Ravasio, F. Langenhorst, R. M. Bolis, E. Granados, S. Hok, T. Kroll, M. Sikorski, T.-C. Weng, H. J. Lee, B. Nagler, T. Sisson, Z. Xing, D. Zhu, G. Giuli, W. L. Mao, S. Glenzer, D. Sokaras, and et al., Ultrafast structural response of shock-compressed plagioclase, Meteoritics Planetary Sci. **57**, 635 (2022).

[60] J. Hernandez, G. Morard, M. Guarguaglini, R. Alonso-Mori, A. Benuzzi-Mounaix, R. Bolis, G. Fiquet, E. Galtier, A. E. Gleason, S. Glenzer, F. Guyot, B. Ko, H. J. Lee, W. L. Mao, B. Nagler, N. Ozaki, A. K. Schuster, S. H. Shim, T. Vinci, and A. Ravasio1, Direct observation of shock-induced disordering of enstatite below the melting temperature, Geophys. Res. Lett. **47**, e2020GL088887 (2020).

[61] R. Jeanloz, T. J. Ahrens, J. Lally, G. L. Nord, J. J. M. Christie, and A. H. Heuer, Shock-Produced Olivine Glass: First Observation, Science **197**, 457 (1977).

[62] D. Kim, S. J. Tracy, R. F. Smith, A. E. Gleason, C. A. Bolme, V. B. Prakapenka, K. Appel, S. Speziale, J. K. Wicks, E. J. Berryman, S. K. Han, M. O. Schoelmerich, H. J. Lee, B. Nagler, E. F. Cunningham, M. C. Akin, P. D. Asimow, J. H. Eggert, and T. S. Duffy, Femtosecond X-Ray diffraction of laser-shocked forsterite (Mg_2SiO_4) to 122 GPa, J. Geophys. Res.: Solid Earth **126**, e2020JB020337 (2021).

[63] S.-H. Shim, B. Ko, D. Sokaras, B. Nagler, H. J. Lee, E. Galtier, S. Glenzer, E. Granados, T. Vinci, G. Fiquet, J. Dolinschi, J. Tappan, B. Kulka, W. L. Mao, G. Morard, A. Ravasio, A. Gleason, and R. Alonso-Mori, Ultrafast x-ray detection of low-spin iron in molten silicate under deep planetary interior conditions, Sci. Adv. **9**, eadi6153 (2023).

[64] S. Zhao, B. Li, B. Remington, C. Wehrenberg, H. Park, E. Hahn, and M. Meyers, Directional amorphization of covalently-bonded solids: A generalized deformation mechanism in extreme loading, Mater. Today **49**, 59 (2021).

[65] R. C. Liebermann and E. Schreiber, Elastic constants of polycrystalline hematite as a function of pressure to 3 kilobars, J. Geophys. Res. **73**, 6585 (1968).

[66] P. Schouwink, L. Dubrovinsky, K. Glazyrin, M. Merlini, M. Hanfland, T. Pippinger, and R. Miletich, High-pressure structural behavior of α-Fe_2O_3 studied by single-crystal x-ray diffraction and synchrotron radiation up to 25 GPa, Am. Mineral. **96**, 1781 (2011).

[67] I. Saeki, T. Ohno, D. Seto, O. Sakai, Y. Sugiyama, T. Sato, A. Yamauchi, K. Kurokawa, M. Takeda, and T. Onishi, Measurement of young's modulus of oxides at high temperature related to the oxidation study, Mater. Sci. Eng. R Rep. **28**, 264 (2011).

[68] C. Meade, R. J. Hemley, and H. K. Mao, High-pressure x-ray diffraction of SiO_2 glass, Phys. Rev. Lett. **69**, 1387 (1992).

[69] G. Morard, J.-A. Hernandez, M. Guarguaglini, R. Bolis, A. Benuzzi-Mounaix, T. Vinci, G. Fiquet, M. A. Baron, S. H. S. B. Ko, A. E. Gleason, W. L. Mao, R. Alonso-Mori, H. J. Lee, B. Nagler, E. Galtier, D. Sokaras, S. H. Glenzer, D. Andrault, G. Garbarino, M. Mezouar *et al.*, In situ X-ray diffraction of silicate liquids and glasses under dynamic and static compression to megabar pressures, Proc. Natl. Acad. Sci. USA **117**, 11981 (2020).

[70] R. J. Hemley, A. P. Jephcoat, H. K. Mao, L. C. Ming, and M. H. Manghnani, Pressure-induced amorphization of crystalline silica, Nature (London) **334**, 52 (1988).

[71] R. G. McQueen and S. P. Marsh, Unpublished Hugoniot data presented by F. Birch, Mem. Geol. Soc. Amer. **97**, 151 (1966).

[72] S. P. Marsh, *Los Alamos Scientific Laboratory Series on Dynamic Material Properties, Shock Hugoniot data* (University of California Press, 1980), Vol. 5.

[73] T. Komabayashi, Thermodynamics of melting relations in the system Fe-FeO at high pressure: Implications for oxygen in the Earth's core, J. Geophys. Res.: Solid Earth **119**, 4164 (2014).

[74] D. Erskine, High pressure Hugoniot of sapphire, AIP Conf. Proc. **309**, 141 (1994).

[75] Y. B. Zeldovitch and Y. P. Raizer, Shock waves in solids, in *Physics of Shock Waves and High-Temperature Hydrodynamic Phenomena* (Elsevier, 1967), pp. 685–781.